

Fluid wetting and penetration characteristics in T-shaped microchannels

Huijie Zhang^{1,3}, Anja Lippert^{2*}, Ronny Leonhardt², Tobias Tolle²,
Luise Nagel^{2,3}, Tomislav Marić^{3*}

¹Mobility Electronics, Robert Bosch GmbH, Markwiesenstrasse 46, Reutlingen,
72770, Germany.

²Corporate Research, Robert Bosch GmbH, Robert-Bosch-Campus 1, Renningen,
71272, Germany.

³Mathematical Modeling and Analysis, Technical University of Darmstadt,
Peter-Gruenberg-Strasse 10, Darmstadt, 64287, Germany.

*Corresponding author(s). E-mail(s): Anja.Lippert@bosch.com;
maric@mma.tu-darmstadt.de;

Abstract

This is the author manuscript of an article Zhang et al. (2024b) published in Experiments in Fluids, available at <https://rdcu.be/dZM07>. Please cite the published journal article Zhang et al. (2024b) when referring to this manuscript. A thorough understanding of media tightness in automotive electronics is crucial for ensuring more reliable and compact product designs, ultimately improving product quality. Concerning the fundamental characteristics of fluid leakage issues, the dynamic wetting and penetration behavior on small scales is of special interest and importance. In this work, four T-shaped microchannels with one inlet and two outlets are experimentally investigated in terms of contact angle dynamics and interface movement over time, generating novel insight into the wetting mechanisms and fluid distribution. With a main channel width of 1 mm, a crevice width of $w = 0.3$ mm, 0.4 mm and a rounding edge radius of $r = 0.1$ mm, 0.2 mm, the geometrical effects on the fluid penetration depth in the crevice and the interface edge pinning effect are analyzed quantitatively using an automated image processing procedure. It is found that the measured dynamic contact angles in all parts can be well described by molecular kinetic theory using local contact line velocities, even with local surface effects and abrupt geometry changes. Moreover, a smaller crevice width, a sharper edge and a larger flow velocity tend to enhance the interface pinning effect and prevent fluid penetration into the crevice. The rounding radius has a more significant effect on the interface pinning compared with crevice width. The experimental data and image processing algorithm are made publicly available.

Keywords: T-shaped microchannel, forced wetting, dynamic contact angle, fluid penetration, interface pinning, automated image processing

1 Introduction

Power electronics play an increasingly vital role, not only in the automotive industry with electrified vehicles, but also in modern energy systems, providing, for example, advantages with respect to power density and efficiency. With rapid development and growing demand of power electronics in industrial applications, yielding a better and more reliable product design has become essential (Wang and Blaabjerg (2021), Yang et al. (2024)). Among all the considered failure models, the fluid penetration and accumulation through unforeseen microfractures along sealing joints or other connection positions have attracted more attention due to its complexity and unpredictability, as reported by Ciprian and Lehman (2009), Hygum and Popok (2015). In particular, while significant progress has been made in the wetting characteristics on small scales, there are still challenges in achieving a comprehensive understanding and predictive modeling concerning geometrically complex leakage scenarios.

Wetting phenomena concern the moving interface between liquids and solids (de Gennes (1985)), which are present in numerous applications and is under active research analytically, experimentally, and numerically, as recently reviewed by Zhang et al. (2023). Contrary to well-studied static wetting, dynamic wetting with contact line (CL) motion is still an active research field, especially in the context of penetration behavior. With extensive research being undertaken in the past decades, several analytical models have been developed to describe CL dynamics. The hydrodynamic theory (HDT) (Voinov (1976), Cox (1986)) concentrates on the macroscopic motion of the fluid interface on the solid substrate, while the molecular kinetic theory (MKT) focuses on the CL friction dissipation in the vicinity of the contact zone on the molecular scale. A combined molecular-hydrodynamic model is proposed by Petrov and Petrov (1992), Brochard-Wyart and de Gennes (1992) and Yang et al. (2020) as a result of the limitations of both models. Furthermore, the interface formation model (IFM) (Shikhmurzaev (1993)) is added to the analytical solution. Widely used empirical models based on experimental findings are given by Jiang et al. (1979) and Bracke et al. (1989).

The T-shaped channel is essential in a wide range of scientific and industrial applications, especially for the phase separation and mixing processes, as reviewed by Yang et al. (2019) and Lu et al. (2022). The gas-liquid two-phase separation mechanism in T-channel is widely utilized due to its simplicity in design and manufacturing, as well as its effective separation capability (Yang et al. (2024)). Speaking of separated two-phase flow in a T-shaped microchannel, the focus of previously published works has been mainly limited to droplet formation (Sivasamy et al. (2011), Wehking et al. (2014)) and breakup mechanisms (Leshansky and Pismen (2009)). However, only few studies have been carried out on addressing the fluid penetration characteristics in a branching-off channel, which has a much smaller width than the inlet channel. The interface pinning effect at the dividing position remains still largely unexplored. An in-depth investigation of this effect expands our understanding of two-phase flow processes in various applications.

While extensive experimental and numerical studies are reported for more controlled wetting dynamics, such as capillary rise (Quéré (1997), Vega et al. (2005)), spreading (Arjmandi-Tash et al.

(2017), Han et al. (2021)) and impinging droplet (Šikalo et al. (2005), Yang et al. (2021)), less attention has been paid to the forced wetting through microchannels, which is of considerable and practical importance in the context of industrial sealing circumstances. In a recent work, Zhang et al. (2024a) experimentally investigated the wetting dynamics of two working fluids through four distinct curved microchannels. The MKT model is reported to be superior to other theoretical approaches in describing the CL movement with local surface effects.

This work reports a comprehensive experimental study on the CL dynamics and penetration characteristics at small capillary numbers Ca ($10^{-6} - 10^{-4}$) through four T-shaped microchannels, distinguished by the crevice width $w = 0.3$ mm, 0.4 mm and rounding radius $r = 0.1$ mm, 0.2 mm. A robust automated image processing method is proposed and utilized to evaluate the dynamic contact angle and interface displacement evolution. The comparison between the measured dynamic contact angles and MKT shows great agreement with physically reasonable fitting parameters, confirming the reliability and reproducibility of the experimental results and image processing method. In addition, the geometrical variations of the channel are found to have an intuitive and significant influence on the penetration depth and edge pinning effect, providing new insights into reliable product design concerning sealing performance.

2 Methodology

2.1 Materials and samples

For the experimental study, chip plates as Topas (a cyclo-olefin copolymer) microscopy slides (Microfluidic Chipshop) are customized with T-shaped open microchannels by micromilling and employed as test samples. One more smooth Topas cover plate is used to enclose the channel by a preload force from the clamping assembly. The geometry and dimensions of the test sample are presented in fig. 1. The manufactured channels have rectangular cross-sections, which are enclosed by side walls (width 0.5 mm, height 0.1 mm). No additional glue or sealing materials are used to avoid contamination and ensure the same wetting properties on all walls. Although the fluid infiltration into the joint between the top of the side wall and the cover plate cannot be entirely prevented, as a result of the surface roughness of $Rz = 0.08$ of the original material, the theoretical maximum of the wall-sealing caused leakage is approximately 0.05%. The theoretical maximum fluid leakage is calculate by assuming that the sealing wall is entirely filled with fluid leakage. For the sample with a crevice width $w = 0.4$ mm, the theoretical maximum fluid leakage is determined by calculating the ratio between theoretical flow velocity U_{theo} and the real flow velocity U_{real} , as follows:

$$\frac{U_{\text{real}}}{U_{\text{theo}}} = \frac{A_{\text{theo}}}{A_{\text{real}}} = \frac{0.4 \times 0.4}{0.4 \times 0.4 + 1 \times 0.08 \times 0.001} = 0.0005. \quad (1)$$

Hence, the mass loss from leakage is negligible. The impact of the leakage on the CL dynamics is also negligible, given that this small amount of leakage is concentrated around the contact point at the edge between the side wall and the cover plate, while the CL is a curve that spans the entire width of side edge and the cover plate. With a well-defined clamping assembly regarding force and position, fluid infiltration is rarely detected in most cases. However, it can be observed in some cases at low flow rates and is discussed in detail in section 3.2. It is important to note that the channels are not intended to be sealed permanently, as they need to be re-opened for further investigations, such as cleaning procedures or microscopy analysis. Other bonding methods, such as glue, double-sided tape, and solvent bonding, were tested but ultimately excluded since they

could introduce unknown variables into the system by altering both the channel geometry and the surface properties of the channel walls. Therefore, closing the channels by incorporating a sealing wall was chosen as a more controlled and reliable approach.

As shown schematically in fig. 1, three connector ports are present on the chip plate: one inlet on the left side of the main channel, two outlets on the top of the crevice, and the right side of the main channel. All samples have a constant channel depth of 0.4 mm and a main channel width of 1 mm. They differ in crevice width $w = 0.3$ mm, 0.4 mm and rounding edge radius $r = 0.1$ mm, 0.2 mm, resulting in four sample variations listed in table 1. The visualization region of interest (ROI) is marked as a yellow square in fig. 1.

As working fluid, de-ionized water is used and the physical properties are internally determined and given in table 2.

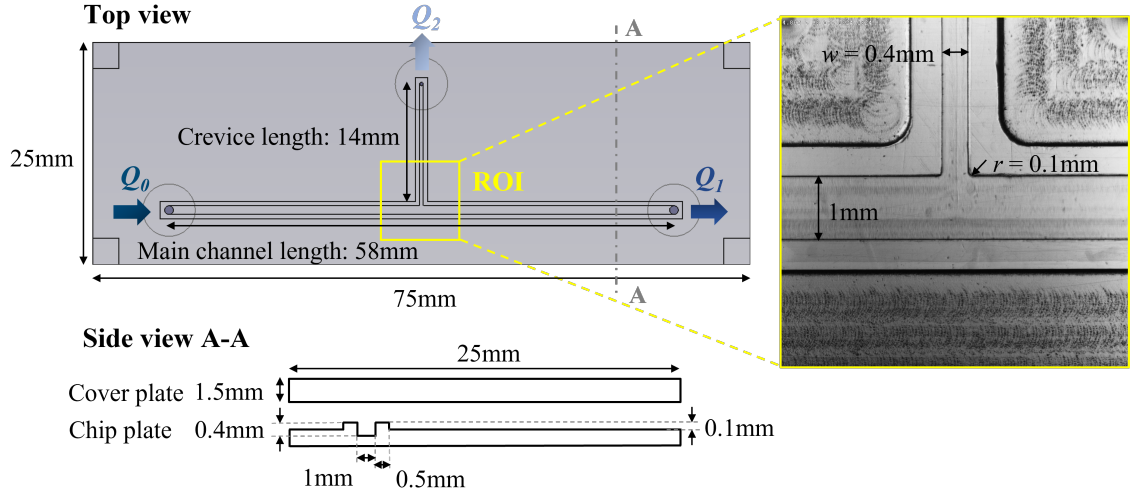


Fig. 1: Chip plate with T-shaped microchannel (crevice width $w = 0.4$ mm, rounding radius $r = 0.1$ mm). Top: top view with region of interest (ROI). Bottom: side view A-A with cover plate.

| Sample | w (mm) | r (mm) |
|-----------|----------|----------|
| w0.4_r0.1 | 0.4 | 0.1 |
| w0.4_r0.2 | 0.4 | 0.2 |
| w0.3_r0.1 | 0.3 | 0.1 |
| w0.3_r0.2 | 0.3 | 0.2 |

Table 1: The test sample variations with crevice width w , rounding edge radius r .

| Working fluid @ 22 °C | density ρ (kg/m ³) | dyn. viscosity μ (Pa · s) | surface tension σ (N/m) |
|--------------------------|--|----------------------------------|-----------------------------------|
| Water | 998.03 | 1.000e-3 | 72.74e-3 |

Table 2: Physical properties of the working fluid and surface tension with air.

2.2 Experimental setup and procedure

The experimental setup is shown in fig. 2 with the test bench on the left side, a zoom-in view in the middle and the chips with clamping assembly on the right side. The clamping assembly consists of two parts to ensure a plane and reproducible force: the top for placing the cover plate and the bottom for the chip plate. Both parts of the clamping assembly are connected with alignment pins and eight equally distributed screws. The clamping force is controlled using a torque wrench. A syringe pump (CETONI Nemesys S) is used to control the inlet fluid flow and the moving interface is captured optically by a high-speed camera (NX4-S3, LDT). The emitted light from a light source is transmitted through a visualization window of the clamping assembly and the transparent chips directly to the camera.

The ROI is visualized by 1024×1024 pixels with an image resolution of $\Delta x = 5.4 \times 10^{-6}$ m. The investigated volumetric flow rates Q_0 and corresponding recorded frame rates are listed in table 3. The data acquisition is realized with MotionStudio.

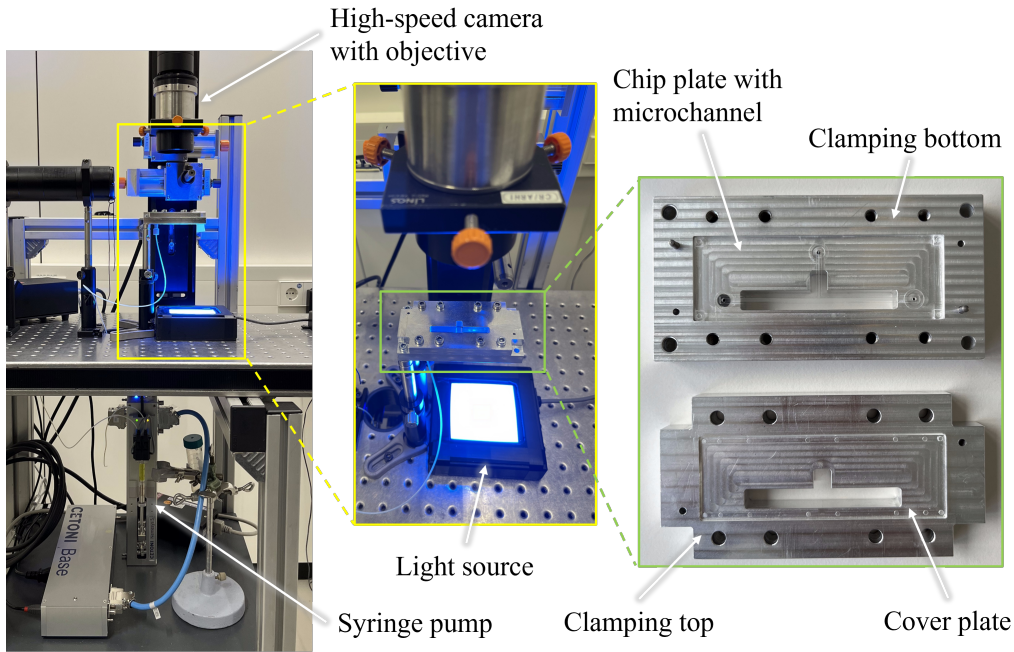


Fig. 2: Experimental setup. Left: test bench. Middle: zoom-in view. Right: chip plate and cover plate with clamping assembly.

The static contact angle (CA) of the sample material is firstly determined as $\theta_0 = 93 \pm 5^\circ$ by placing a water droplet with a volume of $V = 1 \mu\text{L}$ on the chip surface after micromilling. For all operation points, the working fluid is pumped through the inlet port into the main channel with a constant volumetric flow rate Q_0 and leaves the system via the outlet in the crevice with Q_2 and the outlet in the main channel with Q_1 , as denoted in fig. 1. After each test, the clamping assembly is opened and the chips are cleaned with water and dried with compressed air. Each

| Q_0 (ml/s) | U (mm/s) | Ca | Frame rate (fps) |
|--------------|------------|---|------------------|
| 0.0002 | 0.5 | 6.88×10^{-6} | 30 |
| 0.0004 | 1 | 1.37×10^{-5} | 60 |
| 0.002 | 5 | 6.88×10^{-5} | 100 |
| 0.003, 0.004 | 7.5, 10 | 1.03×10^{-4} , 1.37×10^{-4} | 200 |
| 0.006 | 15 | 2.06×10^{-4} | 400 |

Table 3: Investigated volumetric flow rates Q_0 , flow velocities U , capillary numbers Ca in experiments and the corresponding optical frame rates.

test is repeated three times to ensure the reproducibility and accuracy of the results. The image recording is manually started before the interface enters the ROI and stopped after the interface leaves the crevice in the ROI. After the image acquisition, the image series are processed for the CA measurement and interface movement over time via an automated workflow (section 2.3).

2.3 Automated image processing

As mentioned in section 2.2, the dynamic CA and temporal evolution of interface displacement are derived from the recorded images. For accurate and standardized data processing, an automated workflow is proposed as displayed in fig. 3 and publicly available on GitHub (Robert Bosch GmbH (2024)) and TUDDataLib (Zhang et al. (2024-08-19)). The procedure is explained hereafter in four steps and validated in section 3.1.

(i) Define area of interest

Due to the T-shaped geometry, the area of interest for further processing needs to be determined first. For the CA measurement, three areas named “upstream”, “downstream” and “crevice” excluding the T-junction, are chosen for the stable and symmetrical interface shape (fig. 3(a)). For the interface tracking, different areas of interest are selected. To enable continuous tracking along the main channel and the crevice, the areas “x-axis” and “y-axis” are chosen (fig. 3(b)). It is worth mentioning that the exact position of the clamping assembly might vary slightly in each sample change due to the tolerance of holder screws. Therefore, the preliminary selection of all areas of interest is made slightly larger than the expected dimension as shown in fig. 3(a) and (b).

(ii) Wall detection

With the preliminary areas of interest being chosen, the wall edges are detected on the first image of the series as the first two darkest pixels along ten vertical lines in horizontal areas or ten horizontal lines in vertical areas. The coordinates’ median value of the sampled darkest pixels are considered as reference wall edges and then updated as final areas of interest (fig. 3(c) and (d)) for the rest of the images, where the interface is detected for further analysis.

(iii) Interface detection

Within the final areas of interest, the interface is considered to contain the darkest pixels and can be approximated with a polynomial fit. The Random Sample Consensus (RANSAC) developed by Fischler and Bolles (1987) is utilized using `scikit-learn` library for performing the polynomial fit and filtering outliers, for example, scratches or imprints on the sample might be detected as

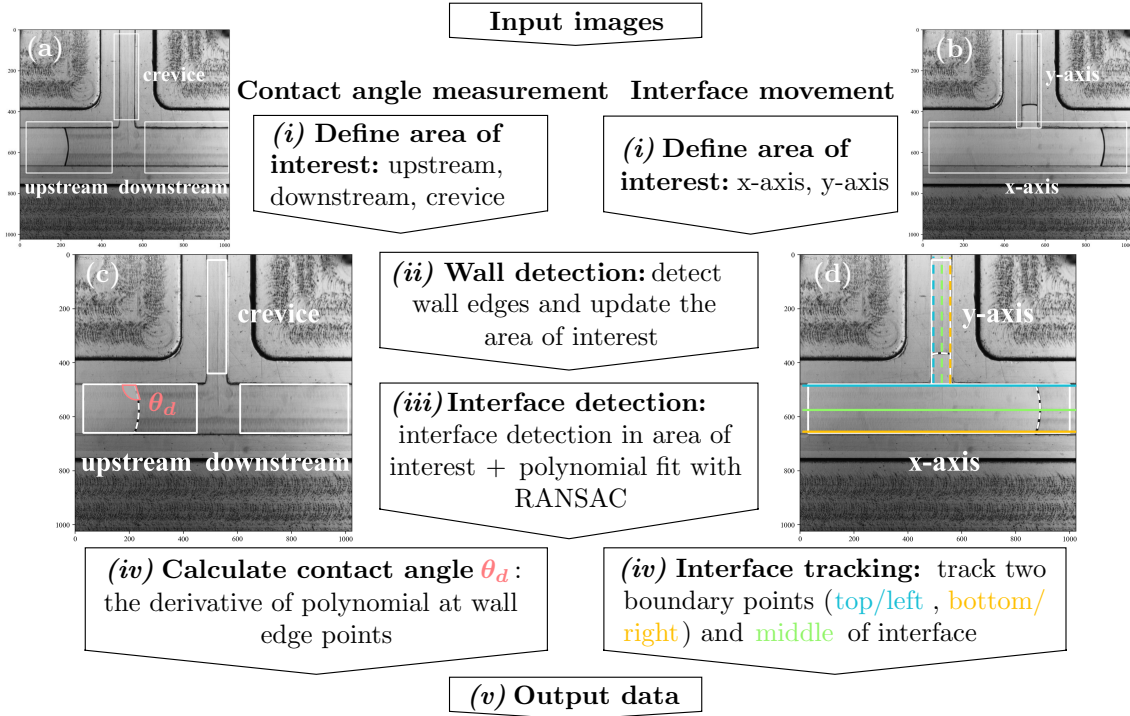


Fig. 3: Automated image processing workflow.

outliers. This approach follows the methodology described by Nagel et al. (2024), where RANSAC was successfully applied to achieve robust polynomial fits in the presence of outliers. The fitted interface is marked as a white dashed curve in fig. 3(c) and (d). A polynomial degree of three is shown to be very robust and accurate for the interface approximation, as confirmed by the low deviation of the statistical results and also by Nagel et al. (2024).

(iv) Calculate contact angle

After the interface is acquired, the CA is calculated in a global approach with the derivative of the polynomial at intersection points between walls and polynomial, as displayed in fig. 3(c).

(iv) Interface tracking

Two boundary points and the middle point of the interface, as marked in fig. 3(d), are tracked to quantify the interface movement over time. The two boundary points are chosen to be three pixels away from the wall edges to exclude the local wall effects. Once the coordinates of the three points are determined, the temporal evolution of the interface displacement can be computed using the image resolution and optical frame rate information.

(v) *Output data*

As output, the CA measurements in “upstream”, “downstream”, “crevice”, and the interface displacement in “x-axis”, “y-axis” areas are saved as CSV files and can be used for further data visualization.

The proposed image processing method provides an automated, robust and transferable workflow for deriving the CA and tracking the interface motion. There are four adjustable parameters in the algorithm: the threshold value for classifying the pixel values `thres`, the number of lines for the channel wall detection `n_lines`, the polynomial degree for the interface fitting `poly_degree` and the number of offset pixels to the wall edges `n_pixels` for the interface tracking. All four parameters are confirmed to be non-sensitive and kept the same for all data sets as `thres = 50`, `n_lines = 10`, `poly_degree = 3` and `n_pixels = 3`.

3 Results and discussion

3.1 Flow rate distribution

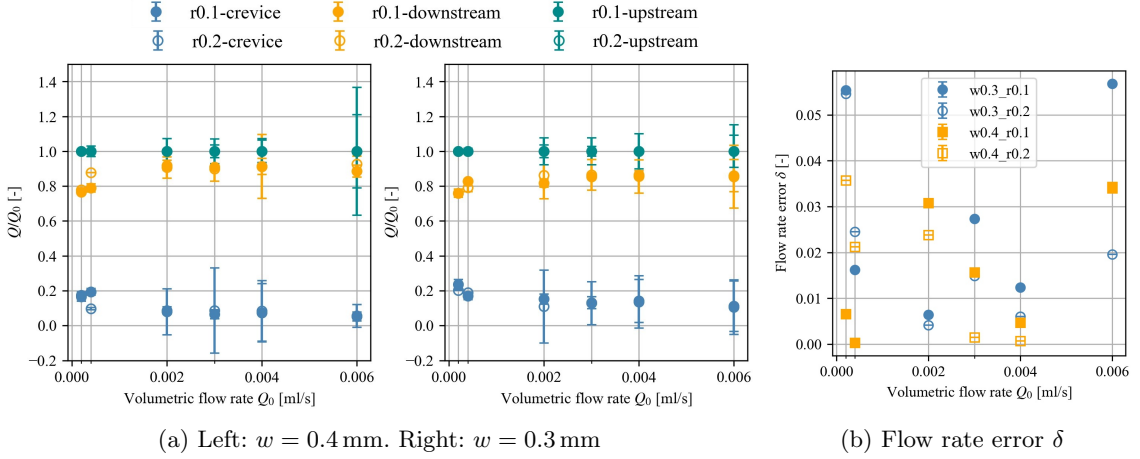


Fig. 4: Flow rate distribution Q/Q_0 with Q as the volumetric flow rate in the “upstream”, “downstream” and “crevice” region and the flow rate error δ (eq. (2)).

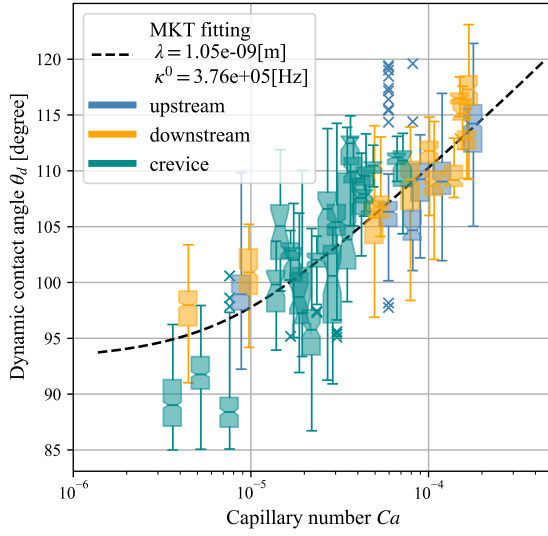
For the validation of the image processing method, the volumetric flow rate distribution in the T-shaped channel is evaluated, and the results are presented in fig. 4a. Q denotes the volumetric flow rate in the “upstream”, “downstream” and “crevice” region and is calculated with the area of the channel cross-section A and the interface velocity U as $Q = A \times U$. It can be seen in fig. 4a that with smaller crevice width w , the amount of the delivered fluid into the crevice is decreasing, while it is increasing along the main channel. To quantify the validity and accuracy of the image

processing workflow, an error indicator δ based on the mass conservation is introduced as

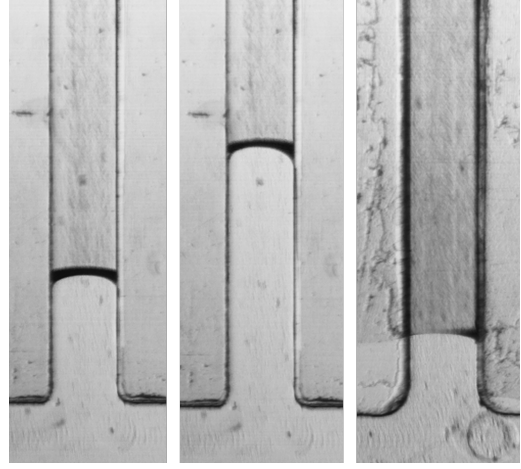
$$\delta = \frac{Q_0 - Q_1 - Q_2}{Q_0}, \quad (2)$$

where Q_1 and Q_2 are the flow rates as denoted in fig. 1. The low error values in fig. 4b confirm that the experimental results are highly reliable and reproducible. The automated image processing method accurately captures flow velocities so that also the calculated volumetric flow rates, with minimal deviation from theoretical expectations.

3.2 Dynamic contact angle



(a) Areas of interest: “upstream”, “downstream” and “crevice”



(b) Examples of thick and asymmetrical interfaces in the “crevice” area

Fig. 5: Dynamic contact angle θ_d versus capillary number Ca with MKT fitting ($\lambda = 1.13 \pm 0.03$ nm, $\kappa^0 = 225.73 \pm 43.58$ kHz) as box plots. The lines inside the boxes mark the median and the interquartile range (IQR), indicated by the boxes, represents the middle 50% (25%-75%) of the data. The whiskers extend to the lowest and highest data points within 1.5 times the IQR, with a few outliers plotted as “x” individually beyond this range.

To further validate the efficiency of the image processing algorithm, the resulting CA measurements are compared to a scientifically proven CA model - MKT model

$$\theta_d = \cos^{-1} \left(\cos \theta_0 - \frac{2k_B T}{\sigma \lambda^2} \sinh^{-1} \left(\frac{U}{2\kappa^0 \lambda} \right) \right), \quad (3)$$

where θ_d is the dynamic CA, k_B is the Boltzmann constant, T is the temperature and U is the interface velocity. The molecular motion frequency at equilibrium κ^0 and the average distance between active sites λ are treated as free parameters and can be estimated via applying curve-fitting on the experimental data. Generally, λ is in the order of molecular dimensions for small molecules from Å to nm and κ^0 varies within several orders of magnitude from kHz to GHz as reported by Duvivier et al. (2013) and Sedev (2015).

The CL velocities are assumed to equal the interface motion velocities determined in section 3.1. Figure 5a compares the dynamic CA from experiments and MKT fitting results as box plots, where a great agreement is visible with physically reasonable parameters. The curve fitting applied on the median values is realized using Python with the SciPy library developed by Virtanen et al. (2020). The dynamic CA shows a strong dependency on the CL capillary number Ca , and the median values increase by around 20 degrees in the investigated Ca range. A larger CA deviation in the “crevice” area can be observed compared to the “upstream” and “downstream” regions, which might be attributed to the smaller width. The small dimension of the crevice could amplify the visualization of the local effects, leading to a more frequent interface pinning and thicker interface, as shown in fig. 5b. Furthermore, the occurrence of leakage (water infiltration between the plates) changes the wetting properties of channel walls and exhibits with the passing interface more of a 90° angle (the rightmost crevice of fig. 5b), especially at small flow rates.

3.3 Penetration depth

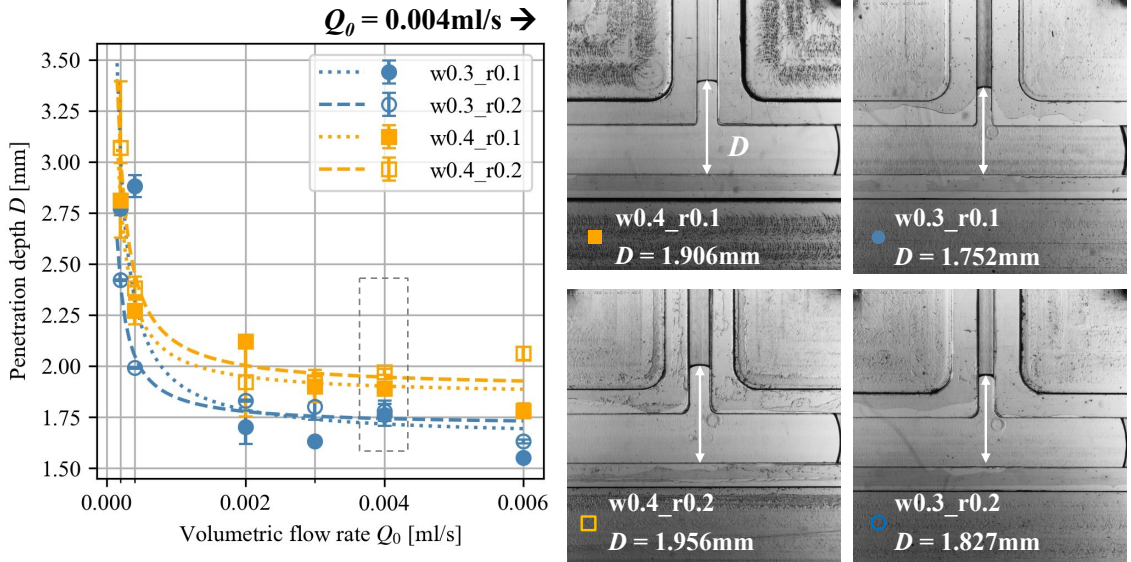


Fig. 6: Left: Penetration depth D in the crevice versus volumetric flow rate Q_0 . Right: $Q_0 = 0.004$ ml/s

The penetration depth of the interface in the crevice D is defined as the distance between the interface in the crevice and the bottom wall of the main channel, when the interface in the main

channel is just about to leave the ROI, as depicted in fig. 6. The left of fig. 6 shows the decrease of the penetration depth D with increasing flow rate Q_0 and decreasing crevice width w . A linear regression analysis between $1/Q_0$ and D is performed using the least squares method to better understand the influence of channel geometry on the penetration depth. Regarding the effect of the rounding edge radius r , a larger r tends to give rise to D , with the exception that for smaller Q_0 , the correlation can be reversed. For example, the samples with crevice width $w = 0.3$ mm at $Q_0 = 0.0002$ ml/s and $Q_0 = 0.0004$ ml/s. This phenomenon can be associated with the fluid infiltration at the joint of both plates due to the manufacturing tolerances, driven by capillary forces. Specifically, a larger r and smaller Q_0 increase the pinning time of the interface top on the left crevice corner (discussed in section 3.4.2), thereby lead to the fluid infiltration into the joint more pronounced and reduce the penetration depth D . In general, a slowly advancing interface is more sensitive to local surface effects, leading to a more irregular interface movement and penetration behavior.

3.4 Pinning effect

Due to the T-junction, the flow is divided into two directions with decreased velocities: one continues the main channel, while the other flows into the orthogonal crevice. It is worth mentioning that due to the rounding radius, “pinning” in this work does not imply that the CL remains completely stationary. Instead, here it means that the interface moves much slower along the rounded edge compared to its movement before and after passing through the T-junction.

Figure 7 illustrates the interface movement over time along the x-axis and y-axis with $w = 0.4$ mm, $r = 0.1$ mm and $Q_0 = 0.004$ ml/s, which can be classified as three stages: before pinning, pinning and after pinning. At the “before pinning” stage, the interface advances steadily towards the T-junction. The positions of the interface top and bottom overlap in fig. 7 due to the symmetrical interface shape, while the interface center is slightly ahead. At $t_0 = 0.27$ s, the interface top arrives at the left wall of the crevice and starts “pinning” at the rounded corner, whereas the middle and bottom keep moving with a decreased velocity. This pinning effect leads to a maximum distance $dx = 0.347$ mm between the interface top and bottom at $t_1 = 0.34$ s, which occurs just before the interface top reaches the right wall of the crevice. Afterwards, the interface contacts the right corner of the crevice at $t_2 = 0.355$ s, causing the flow Q_0 to split into two directions as Q_1 and Q_2 . Hence, $dt = t_2 - t_0 = 0.085$ s refers to the “pinning” time of the interface top on the left rounded corner. The interface movement over time in the y-direction is displayed on the right side of fig. 7. It begins from the end time of pinning at $t_2 = 0.355$ s with a much smaller velocity compared with “before pinning” stage. Moreover, due to the flow splitting and reduced flow rates, the slope of the interface movement in the “after pinning” phase should go through a minor decline in comparison with “before pinning” phase as well and can be observed in fig. 7. The black dotted line shows the movement of the interface middle position in “before pinning” phase. The plots for two different flow rates are presented in fig. 10. The time T denotes the required time for the interface to flow through the main channel in ROI.

As quantitative means of the pinning effect, three parameters - maximum pinning distance dx , pinning time dt and normalized pinning time dt/T are employed and further investigated in the following subsections.

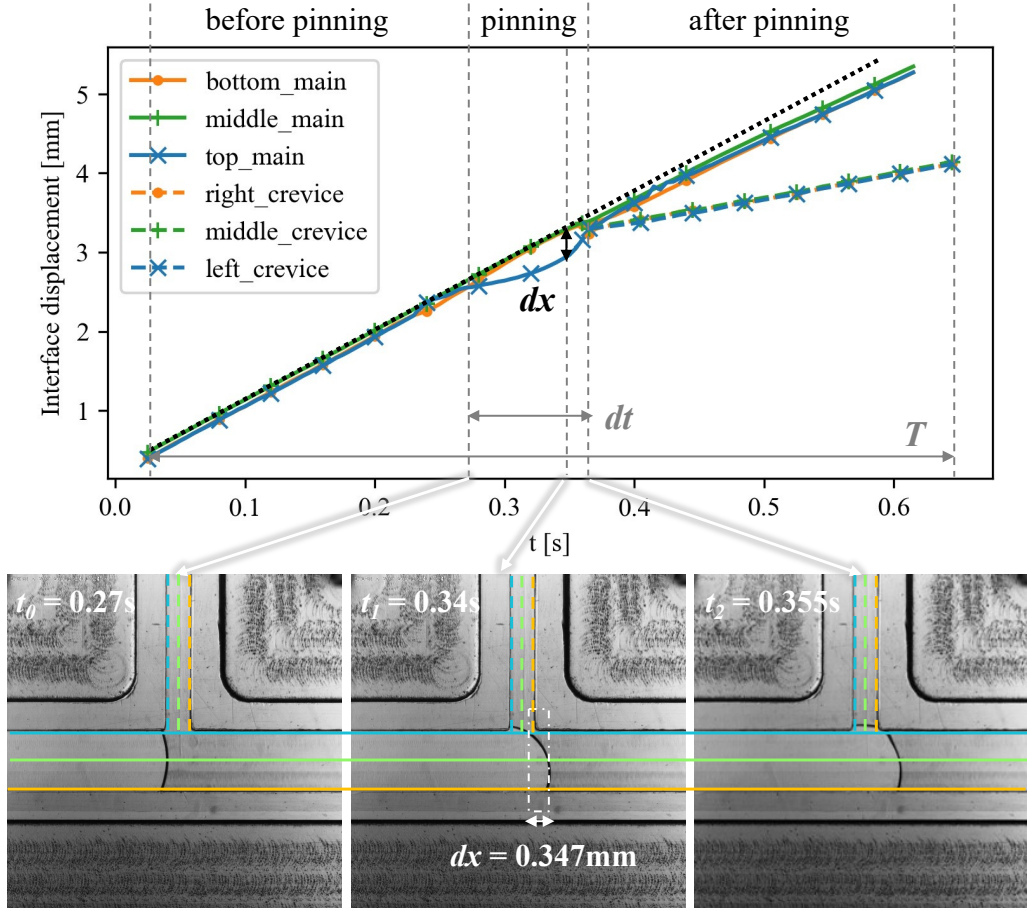


Fig. 7: Top: Interface movement over time with $w = 0.4$ mm and $r = 0.1$ mm at $Q_0 = 0.004$ ml/s. Bottom: Start of pinning at $t = t_0$, maximum pinning distance dx at $t = t_1$, end of pinning at $t = t_2$.

3.4.1 Maximum pinning distance dx

In the left plot of fig. 8, the maximum pinning distance $dx = \max_{t \in T}(x_{bottom}(t) - x_{top}(t))$ exhibits an overall decreasing trend with increasing Q_0 . This behavior is owing to the larger advancing dynamic CA and the resulting interface curvature, leading to a reduced maximum distance dx between the interface top and bottom. Furthermore, a larger rounding radius r allows the interface to progress further along the left wall of the crevice during pinning, resulting in the interface top advancing further ahead and thus a smaller dx . On the contrary, with a larger crevice width w , the dx increases. Interestingly, the influence of a larger rounding r appears to be more significant in decreasing the dx compared with the effect of a smaller w . These trends are more apparent with the overlaid linear fits between Q_0 and dx in fig. 8. The right-hand side of fig. 8 presents the images of the interface with dx marked for an identical flow rate $Q_0 = 0.003$ ml/s, providing a visual confirmation of the relationship between the geometric parameters w , r and dx .

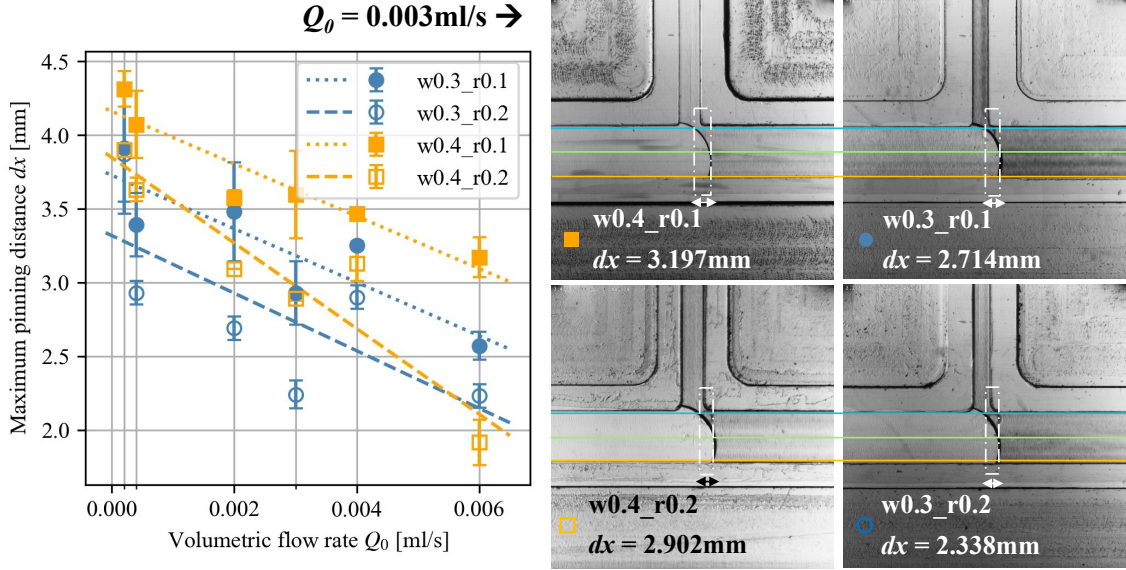


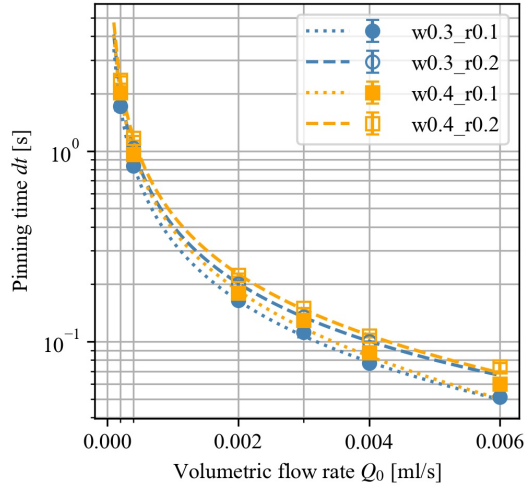
Fig. 8: Left: Maximum pinning distance dx versus volumetric flow rate Q_0 . Right: $Q_0 = 0.003 \text{ ml/s}$.

3.4.2 Pinning time dt and normalized pinning time dt/T

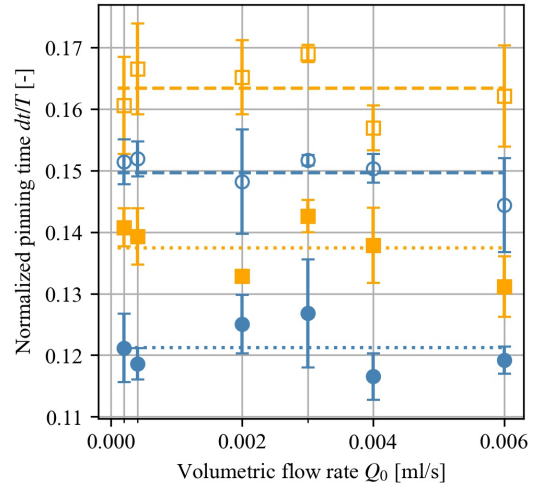
In addition to the maximum pinning distance dx , the interface pinning time $dt = t_2 - t_0$ is analyzed, as displayed in fig. 9a. The start time of pinning t_0 is defined as the time at which the distance between the interface top and bottom reaches or exceeds 30 pixels $|x_{top} - x_{bottom}| \geq 30$ pixels, and this distance continues to increase for the last three frames. This criterion helps to exclude the effect of a potential asymmetric interface shape. The end time of pinning t_2 is defined as the time at which dark pixels appear in the “y-axis” area along the right interface tracking line (orange dashed line in fig. 7).

Similar to dx , a narrower crevice and larger flow rate decrease the pinning time dt . The data analysis reveals the pinning time dt to be inversely proportional to Q_0 . This relationship is intuitive and aligns with the expectations. Figure 9c presents the start and end images of pinning time dt of four samples at $Q_0 = 0.003 \text{ ml/s}$. Interestingly, in contrast to the maximum pinning distance dx , a larger rounding radius tends to increase dt . This trend can be explained by the definition of dt , as mentioned before. It describes the duration during which the interface top starts “pinning” at the left corner, leading to a deviation of the interface from its symmetrical motion, and reaches the right corner of the crevice at the end of “pinning”. With a larger rounding radius r , while having the same crevice width w , the interface pins earlier at the T-junction due to the geometrical conditions and contacts the right corner later, resulting in a longer pinning time. However, this observation does not indicate an enhanced “pinning” effect by the rounding geometry but rather diminished, as evidenced by the evaluation of penetration depth in fig. 6 and maximum pinning distance in fig. 8.

In addition to the pinning time dt , the normalized pinning time dt/T is plotted in fig. 9b. Fitting the data reveals a linear correlation between dt/T and the inflow rate Q_0 . Similar to dt , a larger crevice width w and rounding radius r lead to an increase in dt/T , while it remains independent

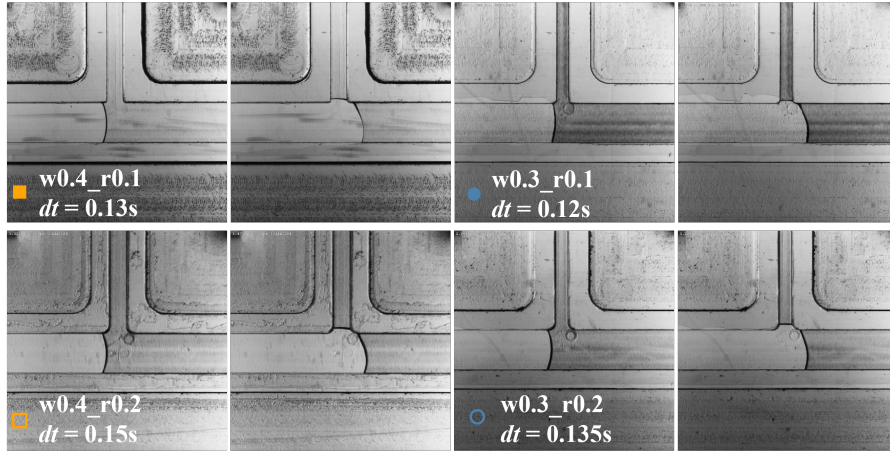


(a) Pinning time dt .



(b) Normalized pinning time dt/T .

$Q_0 = 0.003 \text{ ml/s}$:



(c) Pinning time dt at $Q_0 = 0.003 \text{ ml/s}$ for different crevice widths and rounding edge radii.

Fig. 9: Interface pinning time dt and normalized pinning time dt/T for different volumetric flow rates Q_0 .

of Q_0 . Another noteworthy observation is that both dt and dt/T appear to be more sensitive to the rounding radius r than to the crevice width w . Furthermore, to better represent the effect of the channel geometry on the fluid penetration behavior, a non-dimensional parameter w/r as the ratio between the crevice width and the rounding edge radius is evaluated. However, as a result of

the lack of a clear and significant impact of the ratio w/r on most of the investigated parameters, the plots are included in appendix B.

4 Summary and conclusion

A comprehensive understanding of the wetting and penetration characteristics is essential in reliable product design, particularly regarding sealing performance and corrosion resistance. This work experimentally investigates the geometrical effects on fluid wetting and penetration behaviors in a T-shaped microchannel, consisting of a main channel and an orthogonally placed narrower crevice. The robust and reproducible experimental images are evaluated with an automated image processing method, providing an accurate and straightforward approach to determine the interface motion and the CA at the wall. The algorithm allows to analyze large datasets and reduce the need for manual measurements. Through a systematic evaluation of the results, two main aspects are presented and discussed: the fluid penetration into the crevice and the interface dynamic within the T-junction. The interpretation is based on the results of the automated image processing algorithm, which provides the interface position within the channel and the CA at each time. The algorithm undergoes a sanity check for flow rate conservation and the CAs determined are compared to a scientifically proven CA model. Both show excellent agreement, paving the path for the following evaluations.

The penetration depth D of the interface in the crevice, determined by addressing the interface movement in the “y-axis” area, decreases with smaller crevice width and rounding radius. The data analysis shows an inversely proportional behavior of the penetration depth to the volumetric inflow rate. In terms of the temporal evolution of interface displacement in the “x-axis” area, it can be classified into three stages: before pinning, pinning and after pinning, where the maximum pinning distance dx , pinning time dt and normalized pinning time dt/T are quantified and compared. The first two parameters are shown to decrease with larger flow rates and smaller crevice width, while dt/T remains constant with varying flow rates. On the contrary, dx is inversely proportional to the rounding radius, while dt shows a positive correlation. The rounding radius r contributes more to the pinning effect than the crevice width w . This fact implies that introducing geometric features such as grooves or bends can be more efficient than simply narrowing the sealing joint when aiming for a more reliable product design in terms of sealing performance.

The presented results shed new light on the dynamic wetting and penetration behavior in microchannels with complex geometries from an industrial application perspective. The measured data also allows the determination of the CL dynamics within the parameter space. This enables later numerical investigation by providing the fitted MKT model as a wall boundary condition. In the next step, a numerical framework is to be established along with additional experimental work, to create a large regime map, categorizing a more diverse parameter set in rounding radii, channel widths and materials. Based on data science, we hope to provide correlations that guide future engineers in designing better joint geometries and positions and improving sealing performance. Moreover, as suggested, additional experiments involving other fluids with varying viscosities and surface energies will be conducted. This broader investigation will enhance the applicability of the findings, providing more extensive insights into fluid wetting characteristics across different scenarios and contributing to the development of more robust designs.

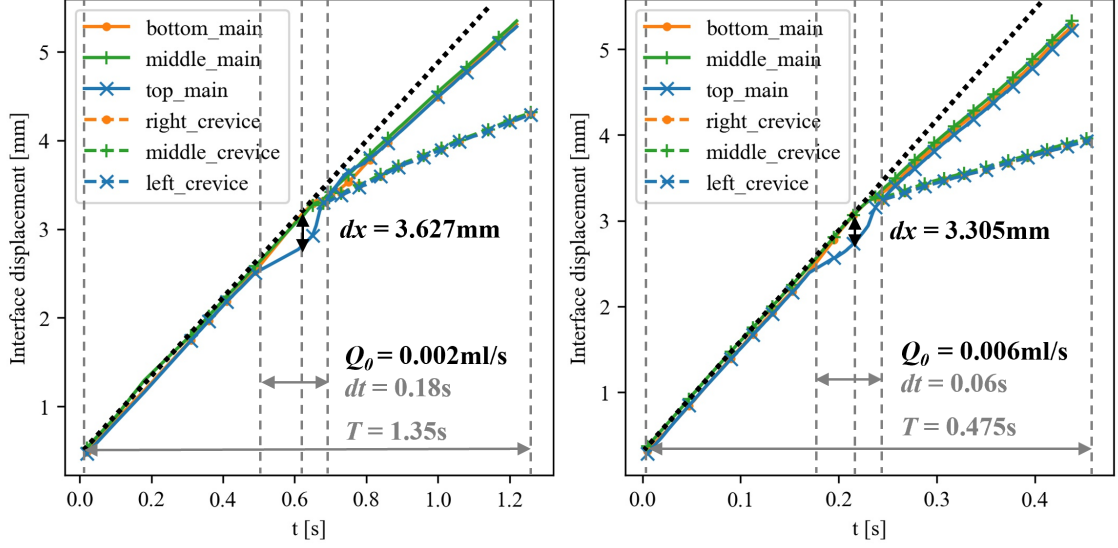


Fig. 10: Interface movement over time of sample with $w = 0.4$ mm and $r = 0.1$ mm at $Q_0 = 0.002$ ml/s and $Q_0 = 0.006$ ml/s.

A Appendix A: Interface displacement over time

The temporal evolution of interface displacement of sample with $w = 0.4$ mm and $r = 0.1$ mm at $Q_0 = 0.002$ ml/s and $Q_0 = 0.006$ ml/s is shown in fig. 10. Similar to fig. 7, the interface movement in the main channel is plotted with that in the crevice superimposed on the right side, beginning from the end of the pinning stage. The results confirm that both the pinning time dt and maximum pinning distance dx decrease with increasing Q_0 . Moreover, the decline in CL velocities after the T-junction, as a result of the flow splitting into two directions, is evident. This behavior is highlighted with the black dotted line as a reference for the change in the interface velocities.

B Appendix B: Non-dimensional parameter w/r

A non-dimensional parameter w/r as the ratio between the crevice width and the rounding edge radius is evaluated, as listed in table 4. The results are presented in fig. 11, with polynomial fits applied to better visualize the impact of the ratio w/r . It should be noted that these polynomial fits are only intended for visualization purposes and do not hold any physical significance. While a positive linear relationship between the maximum pinning distance dx and w/r is apparent, the other three parameters D , dt and dt/T do not exhibit a strong correlation with this ratio w/r . Nevertheless, this aspect w/r is to be incorporated into the future work by including a broader range of channel geometries.

| Sample | w (mm) | r (mm) | w/r |
|-----------|----------|----------|-------|
| w0.4_r0.1 | 0.4 | 0.1 | 4 |
| w0.4_r0.2 | 0.4 | 0.2 | 2 |
| w0.3_r0.1 | 0.3 | 0.1 | 3 |
| w0.3_r0.2 | 0.3 | 0.2 | 1.5 |

Table 4: The test sample variations with crevice width w , rounding edge radius r and the ratio w/r .

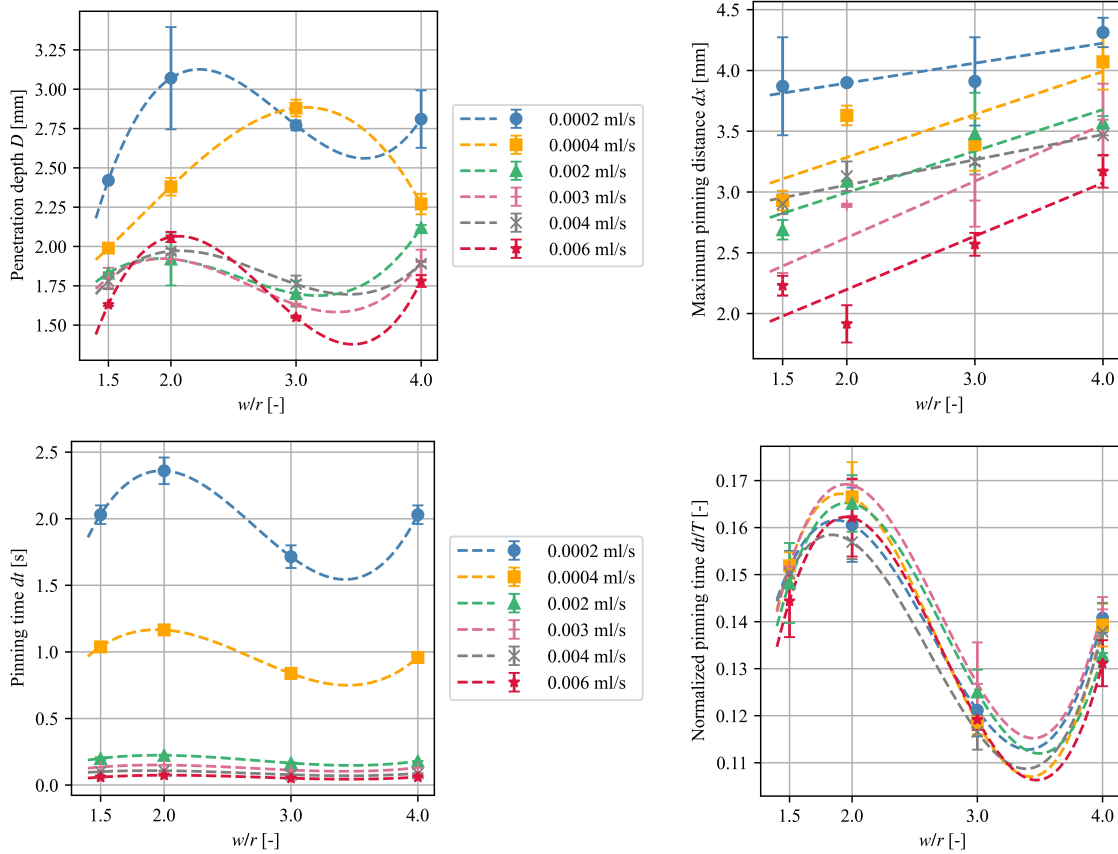


Fig. 11: The penetration depth D , maximum pinning distance dx , pinning time dt and the normalized pinning time dt/T versus the ratio between the crevice width and the rounding radius w/r .

Acknowledgments

The authors would like to thank Dr. Mathis Fricke of Technical University of Darmstadt for the helpful and valuable discussion on the experimental results. The last author acknowledges the

funding by the German Research Foundation (DFG): July 1 2020 - 30 June 2024 funded by the German Research Foundation (DFG) - Project-ID 265191195 - SFB 1194.

References

- Arjmandi-Tash, O., Kovalchuk, N.M., Trybala, A., Kuchin, I.V., Starov, V.M.: Kinetics of wetting and spreading of droplets over various substrates. *Langmuir : the ACS journal of surfaces and colloids* **33** **18**, 4367–4385 (2017)
- Bracke, M., De Voeght, F., Joos, P.: The kinetics of wetting: the dynamic contact angle. In: Bothorel, P., Dufourc, E.J. (eds.) *Trends in Colloid and Interface Science III*, pp. 142–149. Steinkopff, Darmstadt (1989)
- Brochard-Wyart, F., de Gennes, P.G.: Dynamics of partial wetting. *Advances in Colloid and Interface Science* **39**, 1–11 (1992) [https://doi.org/10.1016/0001-8686\(92\)80052-Y](https://doi.org/10.1016/0001-8686(92)80052-Y)
- Ciprian, R., Lehman, B.: Modeling effects of relative humidity, moisture, and extreme environmental conditions on power electronic performance. In: IEEE (ed.) *2009 IEEE Energy Conversion Congress and Exposition*, pp. 1052–1059 (2009). <https://doi.org/10.1109/ECCE.2009.5316423>
- Cox, R.G.: The dynamics of the spreading of liquids on a solid surface. part 1. viscous flow. *Journal of Fluid Mechanics* **168**, 169–194 (1986) <https://doi.org/10.1017/S0022112086000332> . Cited by: 1210
- Duvivier, D., Blake, T.D., De Coninck, J.: Toward a predictive theory of wetting dynamics. *Langmuir* **29**(32), 10132–10140 (2013) <https://doi.org/10.1021/la4017917> . PMID: 23844877
- Genes, P.G.: Wetting: statics and dynamics. *Rev. Mod. Phys.* **57**, 827–863 (1985) <https://doi.org/10.1103/RevModPhys.57.827>
- Fischler, M.A., Bolles, R.C.: Random sample consensus: A paradigm for model fitting with applications to image analysis and automated cartography. In: Fischler, M.A., Firschein, O. (eds.) *Readings in Computer Vision*, pp. 726–740. Morgan Kaufmann, San Francisco (CA) (1987). <https://doi.org/10.1016/B978-0-08-051581-6.50070-2> . <https://www.sciencedirect.com/science/article/pii/B9780080515816500702>
- Hygum, M., Popok, V.: Modeling of humidity-related reliability in enclosures with electronics. In: Kutilainen, J. (ed.) *IMAPS Nordic Annual Conference 2015 June 8-9, Helsingør*, pp. 106–110. Curran Associates, Inc, New York (2015). *IMAPS Nordic 2015 Conference : International Microelectronics And Packaging Society ; Conference date: 01-07-2015*
- Han, T.-Y., Zhang, J., Tan, H., Ni, M.-J.: A consistent and parallelized height function based scheme for applying contact angle to 3d volume-of-fluid simulations. *Journal of Computational Physics* **433**, 110190 (2021) <https://doi.org/10.1016/j.jcp.2021.110190>
- Jiang, T.-S., Soo-Gun, O.H., Slattery, J.C.: Correlation for dynamic contact angle. *Journal*

- of Colloid and Interface Science **69**(1), 74–77 (1979) [https://doi.org/10.1016/0021-9797\(79\)90081-X](https://doi.org/10.1016/0021-9797(79)90081-X)
- Leshansky, A.M., Pismen, L.M.: Breakup of drops in a microfluidic T junction. *Physics of Fluids* **21**(2), 023303 (2009) <https://doi.org/10.1063/1.3078515> https://pubs.aip.org/aip/pof/article-pdf/doi/10.1063/1.3078515/15592015/023303_1_online.pdf
- Lu, P., Zhao, L., Zheng, N., Liu, S., Li, X., Zhou, X., Yan, J.: Progress and prospect of flow phenomena and simulation on two-phase separation in branching t-junctions: A review. *Renewable and Sustainable Energy Reviews* **167**, 112742 (2022) <https://doi.org/10.1016/j.rser.2022.112742>
- Nagel, L., Lippert, A., Leonhardt, R., Tolle, T., Zhang, H., Maric, T.: Experimental and Numerical Study of Microcavity Filling Regimes for Lab-on-a-Chip Applications (2024). <https://arxiv.org/abs/2407.18068>
- Petrov, P., Petrov, I.: A combined molecular-hydrodynamic approach to wetting kinetics. *Langmuir* **8**(7), 1762–1767 (1992) <https://doi.org/10.1021/la00043a013> <https://doi.org/10.1021/la00043a013>
- Quééré, D.: Inertial capillarity. *EPL (Europhysics Letters)* **39**, 533–538 (1997)
- Robert Bosch GmbH: BoschResearch/sepMutliphaseFoam, git tree/publications/ForcedWettingInTJunction. <https://github.com/boschresearch/sepMultiphaseFoam/tree/publications/ForcedWettingInTJunction>. Created: 2024-08-12 (2024)
- scikit-learn: RANSACRegressor. https://scikit-learn.org/stable/modules/generated/sklearn.linear_model.RANSACRegressor.html
- Sedev, R.: The molecular-kinetic approach to wetting dynamics: Achievements and limitations. *Advances in Colloid and Interface Science* **222**, 661–669 (2015) <https://doi.org/10.1016/j.cis.2014.09.008> . Reinhard Miller, Honorary Issue
- Shikhmurzaev, Y.D.: The moving contact line on a smooth solid surface. *International Journal of Multiphase Flow* **19**(4), 589–610 (1993) [https://doi.org/10.1016/0301-9322\(93\)90090-H](https://doi.org/10.1016/0301-9322(93)90090-H)
- Sivasamy, J., Wong, T.-N., Nguyen, N.-T., Kao, L.T.-H.: An investigation on the mechanism of droplet formation in a microfluidic T-junction. *Microfluidics and Nanofluidics* **11**, 1–10 (2011) <https://doi.org/10.1007/s10404-011-0767-8>
- Šikalo, u., Wilhelm, H.-D., Roisman, I.V., Jakirlić, S., Tropea, C.: Dynamic contact angle of spreading droplets: Experiments and simulations. *Physics of Fluids* **17**(6), 062103 (2005) <https://doi.org/10.1063/1.1928828> https://pubs.aip.org/aip/pof/article-pdf/doi/10.1063/1.1928828/14686150/062103_1_online.pdf
- Virtanen, P., Gommers, R., Oliphant, T.E., Haberland, M., Reddy, T., Cournapeau, D., Burovski, E., Peterson, P., Weckesser, W., Bright, J., van der Walt, S.J., Brett, M., Wilson, J., Millman, K.J., Mayorov, N., Nelson, A.R.J., Jones, E., Kern, R., Larson, E., Carey, C.J., Polat, İ., Feng, Y.,

- Moore, E.W., VanderPlas, J., Laxalde, D., Perktold, J., Cimrman, R., Henriksen, I., Quintero, E.A., Harris, C.R., Archibald, A.M., Ribeiro, A.H., Pedregosa, F., van Mulbregt, P., SciPy 1.0 Contributors: SciPy 1.0: Fundamental Algorithms for Scientific Computing in Python. *Nature Methods* **17**, 261–272 (2020) <https://doi.org/10.1038/s41592-019-0686-2>
- Voinov, O.V.: Hydrodynamics of wetting. *Fluid Dynamics* **11**, 714–721 (1976)
- Vega, M.-J., Seveno, D., Lemaur, G., Adão, M.-H., De Coninck, J.: Dynamics of the rise around a fiber: Experimental evidence of the existence of several time scales. *Langmuir* **21**(21), 9584–9590 (2005) <https://doi.org/10.1021/la051341z> . PMID: 16207039
- Wang, H., Blaabjerg, F.: Power electronics reliability: State of the art and outlook. *IEEE Journal of Emerging and Selected Topics in Power Electronics* **9**(6), 6476–6493 (2021) <https://doi.org/10.1109/JESTPE.2020.3037161>
- Wehking, J.D., Gabany, M., Chew, L., Kumar, R.: Effects of viscosity, interfacial tension, and flow geometry on droplet formation in a microfluidic T-junction. *Microfluidics and Nanofluidics* **16**, 441–453 (2014) <https://doi.org/10.1007/s10404-013-1239-0>
- Yang, L., Chen, C., Hu, Y., Wei, F., Cui, J., Zhao, Y., Xu, X., Chen, X., Sun, D.: Three-dimensional bacterial cellulose/polydopamine/tio₂ nanocomposite membrane with enhanced adsorption and photocatalytic degradation for dyes under ultraviolet-visible irradiation. *Journal of Colloid and Interface Science* **562**, 21–28 (2020) <https://doi.org/10.1016/j.jcis.2019.12.013>
- Yang, L., Chen, X., Huang, C., Liu, S., Ning, B., Wang, K.: A review of gas-liquid separation technologies: Separation mechanism, application scope, research status, and development prospects. *Chemical Engineering Research and Design* **201**, 257–274 (2024) <https://doi.org/10.1016/j.cherd.2023.11.057>
- Yang, C., Cao, W., Yang, Z.: Study on dynamic behavior of water droplet impacting on super-hydrophobic surface with micro-pillar structures by vof method. *Colloids and Surfaces A: Physicochemical and Engineering Aspects* **630**, 127634 (2021) <https://doi.org/10.1016/j.colsurfa.2021.127634>
- Yang, B., Su, W., Deng, S., Zhao, L., Lu, P.: State-of-art of branching t-junction: Experiments, modeling, developing prospects and applications. *Experimental Thermal and Fluid Science* **109**, 109895 (2019) <https://doi.org/10.1016/j.expthermflusci.2019.109895>
- Yang, Y., Wang, H., Sangwongwanich, A., Blaabjerg, F.: Chapter 43 - design for reliability of power electronics systems. In: Rashid, M.H. (ed.) *Power Electronics Handbook* (Fifth Edition), pp. 1387–1402. Butterworth-Heinemann, Oxford (2024). <https://doi.org/10.1016/B978-0-323-99216-9.00014-7>
- Zhang, Y., Guo, M., Seveno, D., De Coninck, J.: Dynamic wetting of various liquids: Theoretical models, experiments, simulations and applications. *Advances in Colloid and Interface Science* **313**, 102861 (2023) <https://doi.org/10.1016/j.cis.2023.102861>

- Zhang, H., Lippert, A., Leonhardt, R., Tolle, T., Nagel, L., Fricke, M., Maric, T.: Experimental study of dynamic wetting behavior through curved microchannels with automated image analysis. *Experiments in Fluids* **65**(95) (2024) <https://doi.org/10.1007/s00348-024-03828-7>
- Zhang, H., Lippert, A., Leonhardt, R., Tolle, T., Nagel, L., Marić, T.: Fluid wetting and penetration characteristics in T-shaped microchannels. *Experiments in Fluids* **65**(11), 171 (2024) <https://doi.org/10.1007/s00348-024-03906-w> . Accessed 2024-11-11
- Zhang, H., Lippert, A., Leonhardt, R., Tolle, T., Nagel, L., Maric, T.: Fluid wetting and penetration characteristics in T-shaped microchannels - Data. Technical University of Darmstadt (2024-08-19). <https://doi.org/10.48328/tudatalib-1509> . <https://tudatalib.ulb.tu-darmstadt.de/handle/tudatalib/4306>